MEAM Interatomic Potential for Thermodynamic and Mechanical Properties of Lithium Allotropes

Zheng Qin[a], Rui Wang[a], Songwei Li[a], Tongqi Wen[b], Binglun Yin[c], Zhaoxuan Wu[a,d,*]

[a]*Department of Materials Science and Engineering, City University of Hong Kong, Hong Kong, China*
[b]*Department of Mechanical Engineering, The University of Hong Kong, Hong Kong, China*
[c]*Institute of Applied Mechanics and Center for X-Mechanics, Zhejiang University, 310027 Hangzhou, China*
[d]*Hong Kong Institute for Advanced Study, City University of Hong Kong, Hong Kong, China*

Abstract

Li has relatively simple electronic structure but exhibits complex allotropic phase transitions. Atomistic modelling is important to reveal thermodynamic and mechanical properties at grain and interface scales in multi-phase Li. However, extant interatomic potentials have limited accuracy in reproducing properties in the FCC, BCC and HCP phases of Li. Here, we develop a new interatomic potential for multi-phase Li using the classical MEAM approach. The new potential is fit to key properties of all three phases based on both extant and new DFT calculations. An extensive range of simulations are performed to validate the new potential. Good accuracy and transferability are demonstrated in all three phases and over a wide range of temperatures. The current potential is thus suitable for modelling both thermodynamic and mechanical behavior of Li and can be applied generally in a wide range of applications.

1. Introduction

Being the third element in the periodic table, Li has 3 or 4 neutrons, 3 protons and 3 electrons in the 1s and 2s orbitals. This sub-atomic structure makes Li unique in several aspects, such as extraordinarily low density, high specific heat capacity, high reactivity, good conductivity, as well as complex quantum and isotope effects [1]. While the electronic structure of Li is relatively simple, its thermodynamic and mechanical properties are rather complex [2]. Li is shown to undergo several allotropic phase transformations at different temperatures and pressures [3]. At low temperatures and pressures, the ground state of Li is controversial. The classical phase diagram shows that Li has a rhombohedral 9R-structure below 4 K, an FCC structure between 4–70 K and a BCC structure above 70 K. However, recent experiments [1] suggest that the ground structure of Li is FCC and the rhombohedral structure is metastable. Li also exhibits intriguing mechanical behavior. BCC Li has strong elastic and plastic anisotropy, as well as unusual size and temperature effects on plastic yielding in contrast to transition BCC metals [4]. Some of these unusual behavior, such as differences between isotopes, have quantum mechanical origin. Many other properties, including high temperature phase transitions, plastic deformation and microstructure evolution, is less dependent on quantum effects and may be studied using atomistic simulations with empirical or semi-empirical interatomic potentials. For example, atomistic simulations can explicitly model lithiation, deposition or dendrite formation processes [5–8], which are crucial for Li anode design for enhanced safety and cyclic performance.

The validity of atomistic simulations are limited by accuracies of interatomic potentials. Given the relatively simple electronic structure of Li, developing interatomic potentials for Li is perhaps not exceedingly challenging as compared to that for transition metals [9]. In particular, interatomic potentials based on the embedded-atom method (EAM [10]), modified EAM (MEAM [11–13]) or machine learning frameworks may be sufficiently accurate in applications where thermodynamic and mechanical properties are of primary concerns. Nevertheless, existing interatomic potentials have limited capabilities in describing both the FCC and BCC phases of Li. For example, among the 8 interatomic potentials (MEAM [14–18], EAM [19], SNAP [20] and qSNAP [20], see Fig. 1) examined here, only 2 MEAM potentials developed by Kim et al. [14] and Ko et al. [18] have FCC as the ground state structure. The Ko potential reproduces the energy

*Corresponding author
Email address: zhaoxuwu@cityu.edu.hk (Zhaoxuan Wu)

difference between the BCC and FCC structures in agreement with density-functional theory (DFT) calculations, i.e., $\Delta E_c^{\text{BCC-FCC}} = 1.51$ eV/Atom. However, the FCC structure of the Ko potential exhibit mechanical instability; its elastic constants do not satisfy the Born criterion [21] (i.e., $C_{11} < C_{12}$), which contradicts with DFT calculations. The Kim potential has $\Delta E_c^{\text{BCC-FCC}} = 0.3$ eV/Atom, but its BCC structure elastic constants are substantially different (more than 100%) from experimental/DFT values. Ackland et al. [1] also developed a potential for Li. Their potential shows FCC as the ground state as well, but is not currently compatible with the Large-scale Atomic/Molecular Massively Parallel Simulator (LAMMPS [22]). Therefore, extant potentials are not generally available for predictive modelling of allotropic phase transformation and multi-phase structures in Li.

In this work, we develop a new interatomic potential suitable for modelling thermodynamic and mechanical behavior of multi-phase Li. This new potential uses the classical MEAM and is fit to extensive properties of BCC, HCP and FCC Li computed using DFT calculations. The DFT computed properties include equation of states of FCC and BCC Li, generalized stacking fault energy curves and surface decohesion energies of the BCC Li. In the MEAM potential, the parameters are optimised to reproduce these properties using the particle swarm optimisation (PSO [23]) algorithm. The resulting potential can accurately reproduce the fitting properties, and a broad range of properties outside the fitting dataset, including phase transitions, thermal expansion coefficients, dislocation core structures and glide behavior. The new potential thus enables predictive modeling of thermodynamic and mechanical behavior of Li in all three fundamental phases. In the following, we first describe the DFT calculations and fitting procedures, followed by comparisons with existing potentials and further validations with DFT/extant experimental properties.

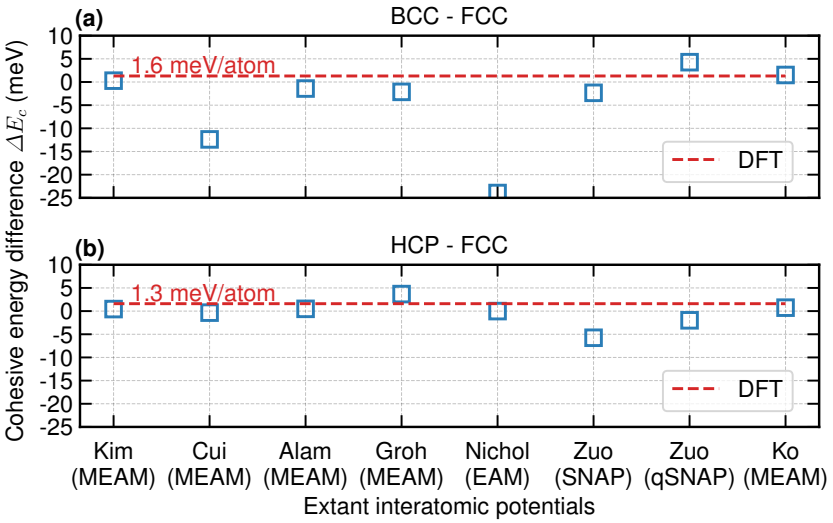

Figure 1: Cohesive energy differences of BCC, HCP and FCC Li. (a) BCC relative to FCC. (b) HCP relative to FCC. The red dashed lines are DFT values and FCC is the ground state structure. The squares are values calculated by extant interatomic potentials for Li (Kim MEAM [14], Cui MEAM [15], Alam MEAM [16], Groh MEAM [17], Nichol EAM [19], Zuo SNAP and qSNAP [20] and Ko MEAM [18]).

2. Computational Methods

2.1. DFT calculations

DFT calculations are performed using the Vienna Ab initio Simulation Package (VASP [24–26]). The exchange and correlation functional is described by the generalized gradient approximation (GGA) with the Perdew-Burke-Ernzerhof (PBE [27]) parameterization. The core electrons are replaced by the projector augmented wave (PAW [28]) pseudopotentials. The $2s$ electrons are treated as the valence-electrons, whose eigenstates are expanded using a plane wave basis set with a cutoff energy of 400 eV. The eigenstate occupancy are smeared using the first-order Methfessel-Paxton method [29] with a smearing parameter of 0.2 eV. In reciprocal space, a Γ-centered Monkhorst-Pack k-mesh [30] is used with a consistent line density of 0.02π Å^{-1} across all geometries. This k-mesh density leads to, for example, $29 \times 29 \times 29$ for Li in the BCC cubic unit cell. Convergence for ionic optimisation is assumed when the atomic forces drop below 1 meV/Å.

Table 1: Supercells used to calculate the surface energy σ, generalized stacking fault energy γ lines and twin boundary energy γ_{tw} by DFT.

Structure	Plane	Supercell vector			Calculation
		$\mathbf{c}_1$	$\mathbf{c}_2$	$\mathbf{c}_3$	
BCC	{100}	[1, 0, 0]	[0, 1, 0]	10[0, 0, 1]	σ
	{110}	[1/2, −1/2, 1/2]	[1/2, −1/2, −1/2]	16[1, 0, 0]	σ, γ
	{112}	[1/2, 1/2, 1/2]	[3/2, −1/2, 1/2]	26[1, 0, 0]	σ, γ
	{112}	[1/2, 1/2, 1/2]	[3/2, −1/2, 1/2]	72[1, 0, 0]	γ_{tw}
	{123}	[1/2, 1/2, 1/2]	[5/2, −1/2, 1/2]	40[1, 0, 0]	σ, γ
FCC	{111}	[1/2, 0, −1/2]	[−1/2, 0, 1/2]	8[1, 1, 1]	γ_{tw}

At large separations, isolated Li atoms possess a magnetic moment of 1 μ_B/atom. Spin-polarized (SP) DFT is thus used in the equation of state (EOS) and cohesive energy calculations for the BCC and FCC structures. SP-DFT is important to obtain accurate cohesive energy of Li. In Bulk Li, no magnetic moment is observed and the spin-unpolarized DFT is used. A tilted-cell method is used to calculate the generalized stacking fault γ-lines. The supercell vectors are shown in Table 1. The details of the tilted-cell method are described in Refs [31–34]. Surface decohesion energy is calculated by incrementally increasing the planar separation d across the selected plane with all ions fixed. For the surface decohesion calculations, the supercell vectors are also shown in Table 1.

2.2. Modified embedded-atom method

The modified embedded-atom method (MEAM) was first proposed by Baskes [11, 12, 35, 36]. In MEAM, the total energy of a system is written as

$$E = \sum_i \left[F_i(\bar{\rho}_i) + \frac{1}{2} \sum_{j \neq i} \phi_{ij}(R_{ij}) S_{ij}^{\phi} \right], \tag{1}$$

where $\bar{\rho}_i$ is the background electron density at site i, F_i denotes the energy of embedding atom i into the background electron density $\bar{\rho}_i$, ϕ_{ij} and R_{ij} are the pair interaction function and distance between atom i and j, S_{ij}^{ϕ} is the multi-body screening function. The outer summation is over all atoms in the system. The contribution of electron density to $\bar{\rho}_i$ and the inner summation include all neighboring atoms of i within a cutoff distance. The electron density $\bar{\rho}_i$ have both a spherically symmetric electron density term and angular-dependent terms. The above functions have analytical expressions with 15 adjustable parameters for a pure element. The MEAM has been widely applied to develop interatomic potentials for various materials, including metals and alloys, as well as semiconductors. Its derivation has been well described in various references (e.g., Ref. [36]). Here, we omit the details, but focus on the fitting procedures, as described below.

2.3. Parameter optimization

For a pure element, developing an MEAM interatomic potential is a complex optimisation problem in 15-dimensional space. In the standard MEAM, all functions are analytical and accuracies of interatomic potentials lie in several key aspects. First, the dataset used for optimising the parameters must include material properties most relevant to the intended application. For thermodynamic and mechanical behavior, the relevant properties include lattice parameter, cohesive energy, equation of state, elastic constants, generalized stacking fault and surface decohesion energies, and vacancy formation energy (Table 2). In the current work, these properties are determined using DFT calculations (see Section 2.1) or extant experimental values, and are used as target properties t_i in the potential fitting process. Second, the algorithm used for optimising potential parameters has to be robust and efficient so that a wide range of parameter space can be searched. We used the PSO algorithm to address this. Third, the target properties provide more data points than the number of variables/degrees of freedom in the potential functions, making the optimisation problem an over-determined system. Interatomic potentials are unlikely to be able to accurately reproduce all target properties. We thus defined an objective function as

$$f = \sum_i^n w_i \left[\frac{p_i - t_i}{t_i} \right]^2 \tag{2}$$

where p_i is the property of the candidate potential and w_i is the weight assigned for each property. Each property is also normalized by the respective target property. The weightage need to be established through

a few trial and error runs. In the current work, high weightage is assigned to the cohesive energies and elastic constants of the FCC, HCP and BCC phases.

Table 2: Weights assigned to individual properties in fitting the interatomic potential parameters via the PSO algorithm.

Structure	Lattice parameter a_0	Cohesive energy E_c	Equation of state EOS	Elastic constant C_{ij}	Surface energy σ	Surface decohesion energy E_{deco}	Vacancy formation energy E_v^f	Stacking fault energy γ_{sf}
BCC	10^4	10^4	10^4	500	10^4 ({110})	10^4 ({110})	10^5	10^6 ({110}), 5×10^5 ({112}), 10^6({123})
FCC	10^4	10^4	-	500	-	-	-	-
HCP	10^4	10^4	-	1	-	-	-	-

In the potential parameter optimisation process, we first generated 12,800 candidate potentials within a predefined parameter space. Each interatomic potential is treated as a particle with 15 degrees of freedom within the PSO algorithm. The parameters in MEAM are thus the coordinates of the particle in the PSO algorithm. The properties p_i of each candidate potential are calculated by calling LAMMPS and the objective function f is computed. All parameters of potential candidates/particle positions $\mathbf{x}_{j+1}$ are updated based on their current position $\mathbf{x}_j$ and updated velocity $\mathbf{v}_{j+1}$ as

$$\mathbf{x}_{j+1} = \mathbf{x}_j + \mathbf{v}_{j+1} \tag{3}$$

where

$$\mathbf{v}_{j+1} = \omega\mathbf{v}_j + \phi_p r_p(\mathbf{p}_j - \mathbf{x}_j) + \phi_g r_g(\mathbf{g}_j - \mathbf{x}_j) \tag{4}$$

where $\mathbf{p}_j$ is the local best position and $\mathbf{g}_j$ is the global best position, which are determined by the objective function in Eq. 2. The parameters ω, ϕ_p and ϕ_g could have effects on the overall optimisation performance, such as the convergence rate. Here we set all three parameters conservatively to 0.5. r_p and r_g are random numbers in the range of $[0, 1]$. The initial particles positions and velocities are randomly assigned within the parameter space.

In the optimisation process, all parameters evolve through iterations as in a regular PSO process. The optimisation completes either when the objective function is below a threshold value or the maximum number of iteration is reached. The weights and parameter space used in this work are provided in Table 2 and 3. In the current study, relatively good potentials can be obtained after 15 iterations.

2.4. Calculations of dislocation core structures and glide behavior in the BCC structure

We use the cluster method to determine the ground state structure of the $a_0/2\langle111\rangle$ edge and screw dislocation cores, where a_0 is the lattice parameter of the BCC lattice. Two cylindrical supercells of radius ~92 Å are first constructed with a BCC lattice oriented as ($x-[111]$, $y-[\bar{1}\bar{1}2]$ and $z-[1\bar{1}0]$) for the screw dislocation and ($x-[\bar{1}\bar{1}2]$, $y-[\bar{1}\bar{1}\bar{1}]$, and $z-[1\bar{1}0]$) for the edge dislocation, respectively. The cylinder axis is always aligned in the x directions and is periodic while other two directions are treated as free surfaces. The supercell lengths (cylinder heights) are $\sqrt{3}a_0$ and $\sqrt{6}a_0$ in the $x-$direction and the supercells contain 7740 and 10938 atoms for the screw and edge dislocation cases, respectively. Dislocations are introduced by applying the atomic displacements of the anisotropic elastic displacement field of the corresponding Volterra dislocations at the cylinder center. Atomic structure optimisation is carried out using a conjugate gradient algorithm with atoms within ~12 Å from the cylinder outer surface fixed to their elastic displacements. Convergence is assumed when the atomic forces drop below 10^{-8} eV/Å.

Dislocation glide behavior is studied using a periodic array of dislocation (PAD) configuration. We first create a supercell of dimensions $(L_x, L_y, L_z) = (\sqrt{3}a_0, 48\sqrt{6}a_0, 41\sqrt{2}a_0)$ and fill the supercell with a BCC lattice oriented as ($x-1/2[111]$, $y-[\bar{1}\bar{1}2]$, $z-[1\bar{1}0]$). Periodic boundary condition is applied in the x and y directions and the z direction is treated as traction-controlled surface. The supercell contains 23616 atoms. The screw dislocation with line direction in the x-axis is introduced by applying the displacement field of the corresponding Volterra dislocation at $(L_y/2, L_z/2)$. A homogeneous shear strain of $\varepsilon_{yx} = |\mathbf{b}|/2 = \sqrt{3}a_0/4$ is applied to the supercell to account for the plastic strain of the screw dislocation [37]. A shear stress σ_{zx} is created by adding forces in the x direction on atoms at the traction-controlled surfaces, i.e., ~12 Å from the upper and lower surfaces.

2.5. Calculations of lattice parameter and elastic constants at finite temperatures

At finite temperatures, lattice parameters a_T and elastic constants C_T are calculated by time-averaging individual properties with a Nosé-Hoover thermostat as implemented in LAMMPS [22]. In particular, we first constructed a fully periodic supercell of perfect crystal. The supercell dimensions are at least 6 nm × 6 nm × 6 nm. The supercell is first equilibrated for 40000 time steps (i.e., 40000 femtoseconds/fs) under stress-free conditions and at respective temperatures using MD simulations with an NPT ensemble. Following equilibration, the simulation box size is measured by averaging its instantaneous size taken at every other time step for 4000 fs under the same NPT ensemble. The lattice parameter is obtained from the simulation box size divided by the number of repeating units. The final lattice parameters reported are the mean value of 10 measurements.

The elastic constants are obtained in a similar, time-averaging scheme. In particular, the same supercell is equilibrated for 16000 time steps under stress-free conditions, followed by applying a ±1% strain in one of the strain components ($\varepsilon_{11}, \varepsilon_{22}, \varepsilon_{33}, \varepsilon_{12}, \varepsilon_{13}, \varepsilon_{23}$). The system is equilibrated again for 16000 time steps using an NVT ensemble with the strain applied. The resulting stress is then measured by averaging the instantaneous stress values taken at every other time step for 4000 time steps under the same NVT ensemble. The final elastic constants are obtained as the mean value of stress divided by the applied strain measured in positive and negative strains.

2.6. Calculations of phonon dispersion relations

The phonon spectra is calculated using PHONOPY [38] and phonoLAMMPS [39]. A supercell of $8[100] \times 8[010] \times 8[001]$ is used for the BCC and FCC structures. The $3N \times 3N$ force matrix (N is the total number of atoms) is first computed using phonoLAMMPS and then used as inputs for Phonopy to obtain the respective phonon spectra.

2.7. Calculations of free energy

The free energies of individual phases are calculated using a non-equilibrium version of the Hamiltonian integration method [40, 41] based on the adiabatic invariance principle [42, 43] and Jarzynski's equality [44] (for details, see Refs. [41, 45]). In the integration, the Hamiltonian of the system is varied continuously from the initial state H_i to the final state H_f along a path described by a coupling function $\lambda(t)$. The Helmholtz free energy difference ΔF between the two states can be estimated from the total work done W given as [44]

$$W = \int_0^{t_s} \mathrm{d}t \dot{\lambda}(t) \frac{\partial H(\lambda)}{\partial \lambda}, \tag{5}$$

where t_s is the switching time and $\dot{\lambda}$ is the time derivative of λ. For an infinitely long switching time t_s, ΔF is simply equal to the total work done. For any finite t_s, the work done becomes a stochastic variable that depends on microscopic initial conditions, and will on average be larger than the free energy difference due to dissipation. For finite t_s, the relation between the free energy difference and total work done can be written as

$$\Delta F = F^f - F^i = \bar{W}_{i \to f} - \bar{E}^{\mathrm{diss}}, \tag{6}$$

where the overbar denotes the average over an ensemble of different initial states, and E^{diss} is the dissipation due to irreversibility caused by finite switching time. Fortunately, the dissipation can be estimated by [46]

$$\bar{E}^{\mathrm{diss}} = \frac{1}{2}[\bar{W}_{i \to f} + \bar{W}_{f \to i}], \tag{7}$$

where $\bar{W}_{i \to f}$ is the work done during forward switching from the initial state to the final state and $\bar{W}_{f \to i}$ is the work done during backward switching from the final state to the initial state. An unbiased estimate of the free energy difference is then

$$\Delta F = F^f - F^i = \frac{1}{2}[\bar{W}_{i \to f} - \bar{W}_{f \to i}]. \tag{8}$$

In the current work, two particular switching paths, namely, Frenkel-Ladd (FL) path [47] and Reversible Scaling (RS) path [48], are used to calculate the temperature dependence of the free energies of FCC, BCC and HCP Li single crystals. The Hamiltonians in the FL and RS paths are

$$H_{\mathrm{FL}}[\lambda(t)] = [1 - \lambda(t)]H_{\mathrm{pot}} + \lambda(t)H_{\mathrm{Einstein}}, \text{ and} \tag{9}$$

$$H_{\mathrm{RS}}[\lambda(t)] = K + \lambda(t)U, \tag{10}$$

where H_{pot} is the Hamiltonian of the potential/real system, H_{Einstein} is the Hamiltonian of the Einstein Crystal (EC), K is the kinetic energy and U is potential energy. The FL path switches the actual system into the EC. Since the free energy of EC is known analytically, the absolute free energy of the system at any temperature can be obtained. The RS path makes a clever choice of the switching path such that the free energy of every intermediate state is related to the free energy of the actual system at another temperature (T/λ). In this way, a continuous variation of the free energy with respect to temperature can be obtained efficiently in a single simulation.

In the above free energy calculation, MD simulations are performed with a time-step size of dt = 1 fs. We use a fully periodic simulation cell of perfect crystals and dimensions of ~5 nm × 5 nm × 5 nm (~7000 atoms). The system is first equilibrated at selected temperatures for 100,000 time steps before both forward and backward switching processes. The switching time for the FL and RS paths are 0.2 ns and 2 ns respectively. Three independent calculations with different initial velocity realizations are performed for each case to estimate and reduce statistical errors. With the above simulation setting, both the dissipation error and the statistical error are kept well below 0.1 meV/atom.

3. Results

3.1. Parameters of MEAM interatomic potentials

Table 3 shows the optimised parameters of the new interatomic potential for Li. In addition, we have provided the parameter files in LAMMPS format in the supplementary materials for direct applications by interested readers.

Table 3: Parameter space and optimised value of the new MEAM interatomic potential for Li developed in this work.

	α	$\beta^{(0)}$	$\beta^{(1)}$	$\beta^{(2)}$	$\beta^{(3)}$	$t^{(1)}$	$t^{(2)}$	$t^{(3)}$	A	C_{min}	C_{max}	d_{repuls}	d_{attrac}	r_{c}	Δr
Upper limit	3.2	3	2	5	4.5	5	4	1	1.3	0.8	3.5	0.15	0.1	8	5.5
Lower limit	2.9	1	0	3	2	4	3	0	0.8	0	2.2	-0.1	-0.1	6	3
Optimised value	3.142	1.785	1.254	4.594	2.940	4.128	3.369	0.267	1.011	0.0006	2.728	0.080	0.005	6.652	4.047

3.2. Basic properties of lithium

We first compare some basic properties of the new interatomic potential with corresponding values from DFT calculations and experiments. Since our goal is to produce a potential accurate for thermodynamic and mechanical behavior of Li, we focus its benchmark with the Ko potential while omitting others. Table 4 shows an extensive set of properties of Li in BCC, FCC and HCP structures. Figure 2 shows a summary of key properties. For all three structures, the new potential accurately reproduces the lattice parameters, cohesive energies, elastic constants and surface energies. For the new potential, all three structures satisfy the Born criteria [21] as in DFT, i.e.,

$$\text{cubic} : C_{11} > C_{12}; C_{11} + 2C_{12} > 0; C_{44} > 0; \text{ and}$$
$$\text{hexagonal} : C_{11} > |C_{12}|; 2C_{13}^2 < C_{33}(C_{11} + C_{12}); C_{44} > 0.$$

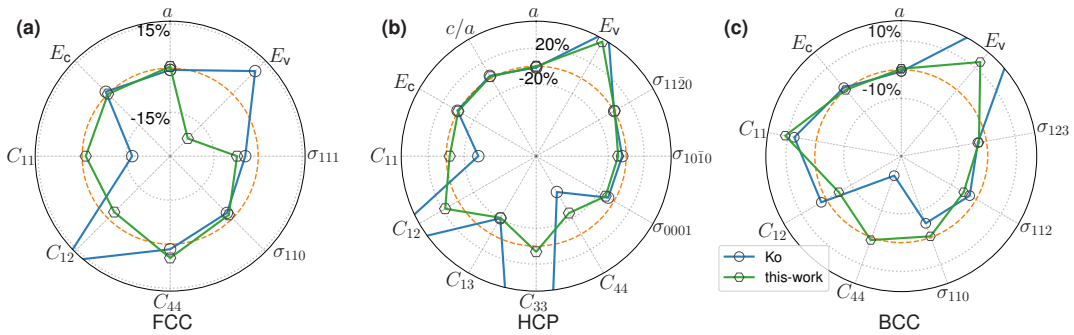

Figure 2: Basic properties of Li in FCC, HCP and BCC structures. The orange dashed lines are DFT/experimental values used as references. The gray dotted lines are relative offsets from the reference values. Some properties of the Ko potential are outside the plotting range. See Table 4 for the definitions of symbols and respective absolute values.

Table 4: Properties of lithium in BCC, FCC and HCP structure. The table compares the lattice parameter a (Å), cohesive energy E_c (eV/atom) and difference ΔE_c (meV/atom), elastic constants C_{ij} (GPa), surface energy σ (mJ/m^2), and vacancy formation energy E_v (eV) among the experiment/DFT values, the new and the Ko potentials. In the 4th column, experimental values are shown with upright font and DFT values are in italic font.

Structure	Property		Experiment/DFT	This work	Ko
FCC	a	0 K	*4.324* [49], *4.3305* [a]	4.347	4.298
		300 K	4.388 [50] (298 K under pressure)	4.418	N.A. [b]
	E_c		*−1.6066* [18], *−1.6106* [a]	-1.63078	-1.6485 [18]
	C_{ij}	C_{11}	*16.22* [1]	16.02	13.45
		C_{12}	*12.51* [1]	12.13	15.09
		C_{44}	*10.43* [1]	10.92	10.61
	σ	{110}	*530* [51]	521	516
		{111}	*500* [51]	464	478
	E_v		*0.6* [52]	0.471	0.666
HCP	a	0 K	*3.058* [49], *3.078* [53]	3.075	3.033
		300 K	3.111 [50] (298 K under pressure)	3.124	2.988
	c/a	0 K	*1.599* [53]	1.631	1.648
		300 K		1.632	1.638
	E_c		*-1.6063* [18], *-1.906* [53]	-1.63073	-1.6478 [18]
	$\Delta E_c^{\text{HCP-FCC}}$		*0.3* [18]	0.05	0.74
	C_{ij}	C_{11}	*22* [54]	21.16	14.15
		C_{12}	*11* [54]	12.85	22.26
		C_{13}	*8* [54]	6.33	6.38
		C_{33}	*26* [54]	27.62	171.79
		C_{44}	*6* [54]	4.38	2.76
	σ	{0001}	*520* [51]	463	480
		$\{10\bar{1}0\}$	*530* [51]	483	507
		$\{11\bar{2}0\}$	*510* [51]	514	510
	E_v		*0.63* [52]	0.940	1.023
BCC	a	0 K	*3.44* [55], *3.436* [17], *3.438* [18], *3.4396* [a]	3.451	3.419 [18]
		300 K	3.51 [56]	3.506	3.477
	E_c		−1.63 [57], *−1.61* [55], *−1.605* [18], *−1.6091* [a]	−1.63024	−1.647 [18]
	$\Delta E_c^{\text{BCC-FCC}}$		1.5 [a]	0.54	1.5
	C_{ij}	C_{11}	14.54 [58], *16.4* [18], *15.04* [1]	16.68	16.20 [18]
		C_{12}	12.16 [58], *15.5* [18], *13.23* [1]	12.57	13.50 [18]
		C_{44}	11.58 [58], *8.5* [18], *11.14* [1]	11.25	8.60 [18]
	σ	{110}	522 [59], *487* [18], *500* [51]	498	474 [18]
		{112}	*540* [51]	513	526
		{123}	*530* [51]	516	514
	E_v		0.34 [60], *0.481* [18]	0.383	0.468 [18]

[a] Calculated by DFT in this work.
[b] For the Ko potential [18], the FCC structure is not stable at finite temperatures.

For the new potential, FCC is the ground state while HCP and BCC are metastable at 0 K. The cohesive energy differences ΔE_c are small (0.5 meV/atom) and at the accuracy of DFT calculations. However, this small ΔE_c is essential and controls the phase transition from FCC to BCC at higher temperatures (discussed below). The potential also predicts a wide range surface energies not included in the fitting dataset (except $\{110\}_{BCC}$). In general, the Ko potential also has accurate properties comparable to the new potential. However, its elastic constants are less accurate in all three phases.

3.3. Equation of state

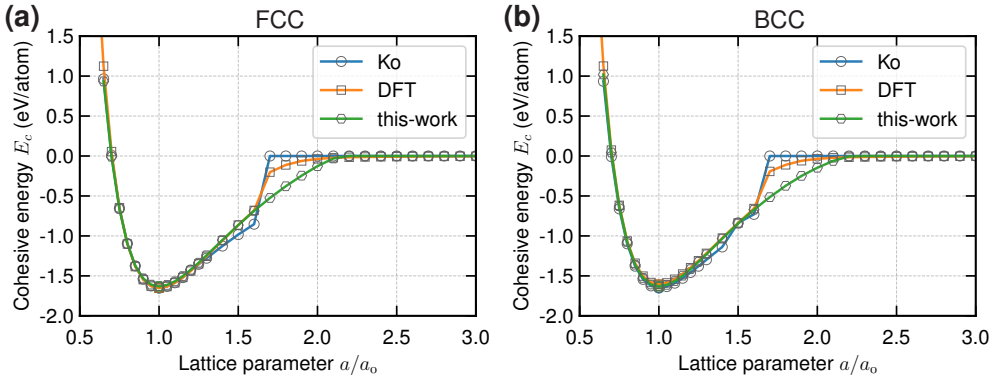

Figure 3: Cohesive energy as a function of lattice parameter. (a) FCC and (b) BCC. In DFT, the cohesive energy has an abrupt change between $1.6a_0$ and $1.7a_0$ as Li atoms become spin-polarized. The Ko potential [18] has a similar abrupt change due to the cutoff in interatomic interactions.

Figure 3 shows the cohesive energy as a function of lattice parameter, i.e., Equation of state (EOS). We focus on the FCC and BCC phases and compare the new potential with DFT and the Ko potential. For both structures and near the equilibrium lattice spacing ($\Delta a = \pm 30\% a_0$), the new potential accurately reproduces the EOS curves, so does the Ko potential. The DFT results show an abrupt change in the cohesive energy between 1.6-1.7a_0 as individual Li atom becomes spin-polarized due to the unpaired electron in the $2s^1$ orbital. The energy variation becomes smooth again beyond $1.7a_0$. The Ko potential also exhibits abrupt energy changes. However, this rapid changes in energy are due to atom separation reaching the cutoff distance of the interatomic potential. While it may appear to be consistent with DFT, the un-smooth change in energy has un-physical impact on other properties/processes when atom separations are increased beyond the cutoff distance, as discussed below. The new potential, however, has smooth variation in energy in the entire range. The classical MEAM does not contain magnetism, which becomes important only when Li atoms are well-separated individually. However, this shortcoming does not affect other properties related to thermodynamic and mechanical behavior in general.

3.4. Surface decohesion

Surface decohesion energy and its gradient give the energy and cohesive stress variation during atomic plane separation. This property is important for accurate modeling of material fracture behavior. Figure 4 shows the surface decohesion energy and its gradient for 4 planes of the BCC structure in comparison with DFT and the Ko potential. The DFT data for the {110} plane is included in the potential fitting dataset while the rest are used for validation. Overall, the new potential reproduces the energy variations, their gradients and peak values well. The Ko potential also has relatively good matching with DFT data. However, it has relatively sharp changes in energy in all 4 cases, leading to un-physical jumps in the gradient/stress at large planar separation. The rapid change in energy/stress is due to the cutoff function in atomic interaction used in the potential, as seen in earlier works as well [61]. This can be addressed by using an extended cutoff smoothing distance Δr, as used in the current new MEAM potential.

3.5. Generalized stacking fault energy

The generalized stacking fault energy line and surface (γ-line/surface) give the energy variation during slip processes along atomic planes. The γ-line/surface profile dictates the energy barrier to nucleate dislocations and their corresponding core structure/dissociation. Figure 5 shows γ-lines in the $\langle 111 \rangle$ direction on the {110}, {112} and {123} planes in the BCC structure. The {110} plane has the lowest unstable stacking fault energy γ_{us}, while the {112} and {123} planes have nearly the same γ_{us}. All γ_{us} on these planes

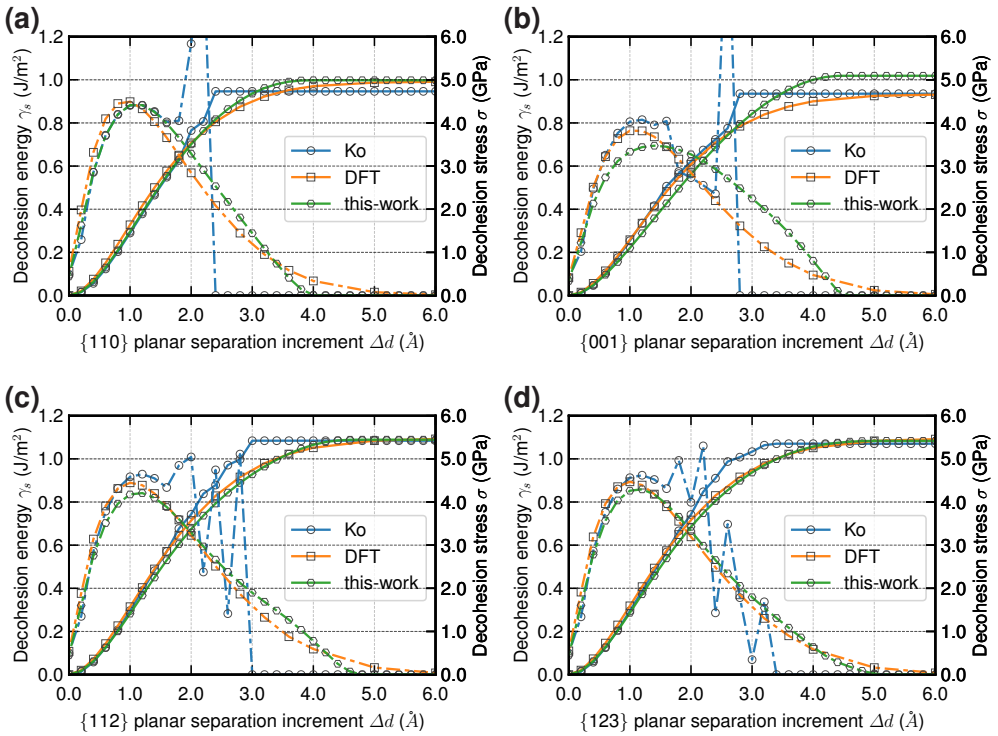

Figure 4: Surface decohesion energy curves of the {110}, {112} and {123} planes in the BCC structure. The Ko potential [18] exhibits abrupt change in decohesion energy and its gradient in all cases due to the cutoff in interatomic interactions.

are much lower than those of transition metals. However, this is not surprising, given the much lower elastic constants of Li (e.g., on the {110} plane, $\gamma_{\rm us}^{\rm Li} \approx 0.07$ J/m^2 vs $\gamma_{\rm us}^{\rm W} \approx 1.7$ J/m^2, $C_{44}^{\rm Li} \approx 11.2$GPa vs $C_{44}^{\rm W} \approx 140$ GPa). The new potential reproduces all the γ-lines and has the same order of $\gamma_{\rm us}$ as that in DFT, i.e., $\gamma_{\rm us}^{\{110\}} < \gamma_{\rm us}^{\{123\}} < \gamma_{\rm us}^{\{112\}}$. Overall, it has better agreement with DFT than the Ko potential.

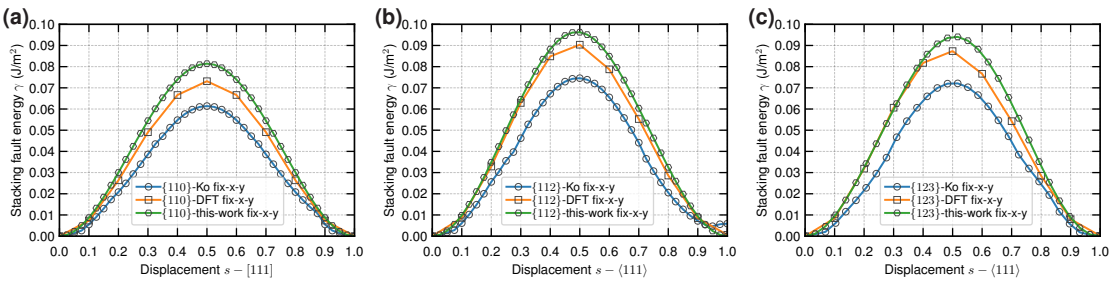

Figure 5: Generalized stacking fault energy (γ) lines of the {110}, {112} and {123} planes in the BCC structure. The γ-lines are calculated by fixing atoms within the slip plane ($x-y$-plane) but allowing out-of-plane (z-direction) relaxation. The new MEAM potential has better agreement with DFT. On the {112} plane, structure change occurs during the shear and relaxation process in the Ko potential and the final energy is slightly higher than that of the perfect crystal.

Figure 6 shows the γ-surfaces of the {110}, {112} and {123} planes in the BCC structure. No meta stable stacking fault is seen in any of the three potential slip planes. The {110}-plane γ surface is also quantitatively similar to that calculated by DFT [9]. Furthermore, all the γ-surfaces are qualitatively similar to those of BCC transition metals. However, on the {110} plane, the low energy valley are more extended in the $\langle 110\rangle$ direction, which has subtle effects on dislocation core structures, as discussed below.

3.6. Twin boundary structures and energies

Twinning can potentially be an important deformation mechanism in FCC and BCC Li. We therefore determine the twin boundary structures and energies using DFT calculations and the current interatomic potential. Figure 7 shows the {111} and {112} coherent twin boundary structures in FCC and BCC. In all the cases, the boundary structures are nearly identical between DFT and MEAM. In the FCC structure, the

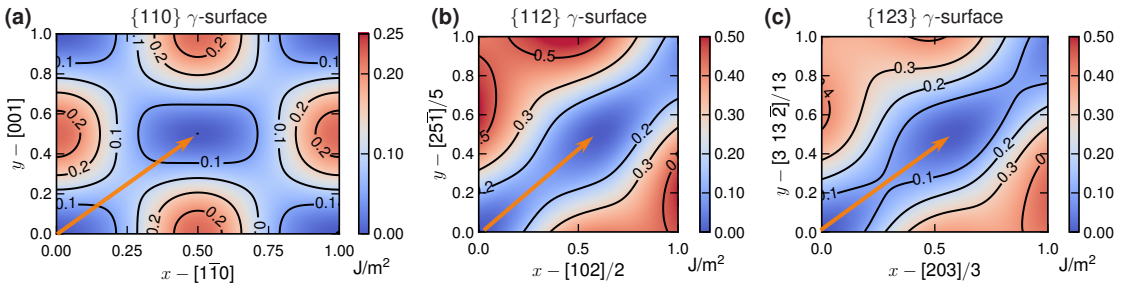

Figure 6: Generalized stacking fault energy (γ) surfaces of the (a) {110}, (b) {112} and (c) {123} planes calculated by the new MEAM interatomic potential. The arrows indicate the shear displacement from one perfect crystal structure to the next one.

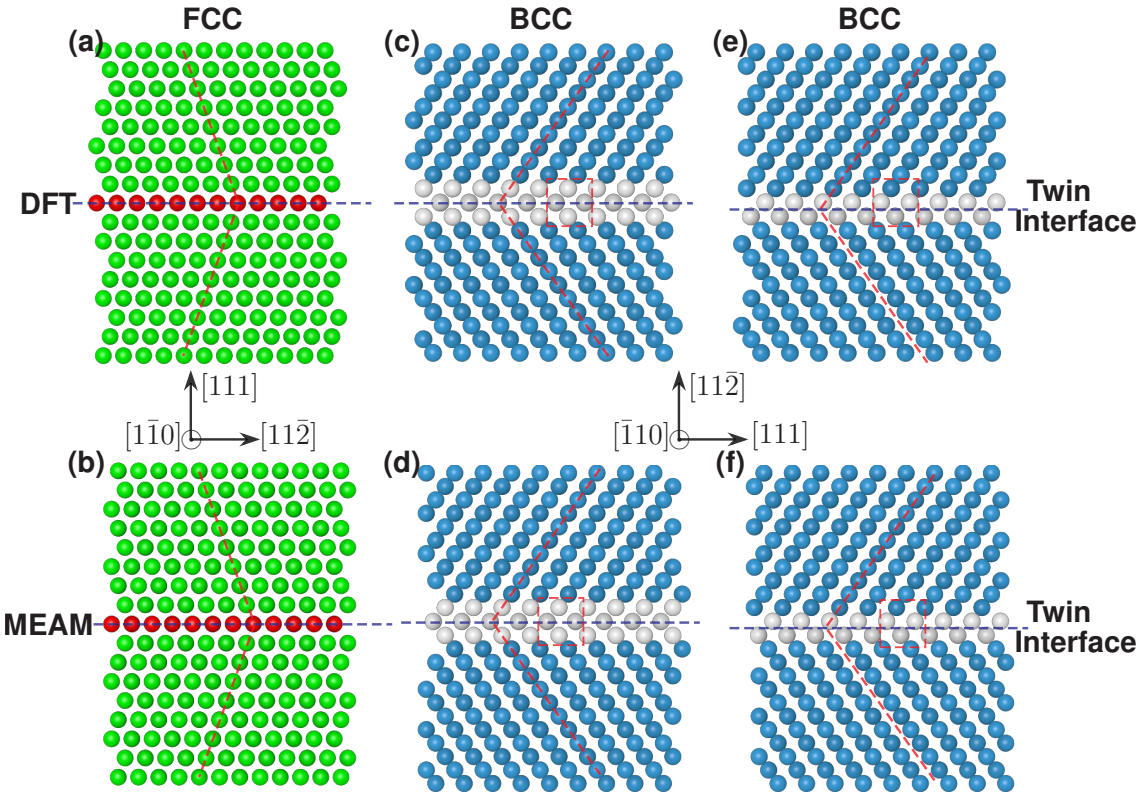

Figure 7: Coherent twin boundary structures in FCC and BCC Li calculated by DFT and the new MEAM potential. (a-b) $\langle 11\bar{2}\rangle\{111\}$ twin with a reflection symmetry about the {111} plane in the FCC structure. (c-d) Symmetric $\langle 111\rangle\{112\}$ twin with a reflection symmetry about the {112} plane in the BCC structure. (e-f) The isosceles $\langle 111\rangle\{112\}$ twin boundary structure in the BCC structure. Atoms are colored based on their local atomic structure identified by the common neighbor analysis (CNA [62]): FCC-green, BCC-blue, HCP-red, others-white.

new potential has the twin interface energy $\gamma_{\text{tw}}^{\{111\}}$ = 0.1 mJ/m^2, lower than $\gamma_{\text{tw}}^{\{111\}}$ = 0.27 mJ/m^2 predicted by DFT. The current potential thus underestimates $\gamma_{\text{tw}}^{\{111\}}$, largely due to its small $\Delta E_{\text{c}}^{\text{HCP-FCC}}$ as compared to the DFT value (Table 4). Between the current MEAM potential and DFT, the discrepancy is relatively large in percentage wise, but the absolute value is small and at the boundary of DFT accuracies. In the BCC structure, the ⟨111⟩{112} twin boundary exhibits two structures: a pure reflection structure (Fig. 7c-d) and an isosceles structure (Fig. 7e-f) as first proposed by Vitek [63]. Similar structures have also been reported in BCC transition metals [64]. The current MEAM potential has $\gamma_{\text{tw ref}}^{\{112\}}$ = 21.96 mJ/m^2 and $\gamma_{\text{tw isos}}^{\{112\}}$ = 21.75 mJ/m^2, while DFT calculations predict $\gamma_{\text{tw ref}}^{\{112\}}$ = 20.67 mJ/m^2 and $\gamma_{\text{tw isos}}^{\{112\}}$ = 20.50 mJ/m^2, respectively. For Li, the symmetric reflection twin boundary is thus expected to be meta-stable relative to the isosceles structure. The new MEAM potential thus accurately reproduces the twin boundary structure, energy and their meta-stability in the BCC structure. These twin boundary structures are not in the potential fitting dataset, but the energy differences are only ~6%, further suggesting the robustness of the current potential.

3.7. Thermal expansion

Figure 8 shows the lattice parameter as a function of temperature for the new potential in comparison with experimental/DFT values and the Ko potential. For the Ko potential, the FCC structure is not stable even at 4 K when using a $16 \times 16 \times 16$ supercell. The new potential has stable or meta-stable FCC structure within 0 K – 450 K. It slightly overestimates the FCC lattice parameter by ~0.6%. Both potentials are stable in the BCC structure within 0 K – 450 K. At low temperatures of 0 – 20 K, The Ko potential has relatively large coefficient thermal expansion (CTE) ($\alpha_{\text{T}} = 1/a(\partial a/\partial T)$) while experimental values suggest $\alpha_{\text{T}} \to 0$ as $T \to 0$ (dictated by the 3rd Law of Thermodynamics). The new potential has nearly constant α_{T} since it is based on classical mechanics and neglects quantum mechanics effects. The potential, however, has accurate lattice constant of the BCC structure at room temperatures. The measured α_{T} are in a range of 40 – 70 $\times 10^{-6}$ K^{-1} below 400 K, close to the experimental value of 56 $\times 10^{-6}$ K^{-1} [65]. Above 400 K (~0.9 T_{m}), α_{T} is more scattered due to limited sampling close to the melting point. Above 500 K, both the FCC and BCC structures are not stable and transform to a liquid structure using the new potential. Overall, the new potential accurately reproduces the lattice parameters across the entire temperature range of Li solid phases.

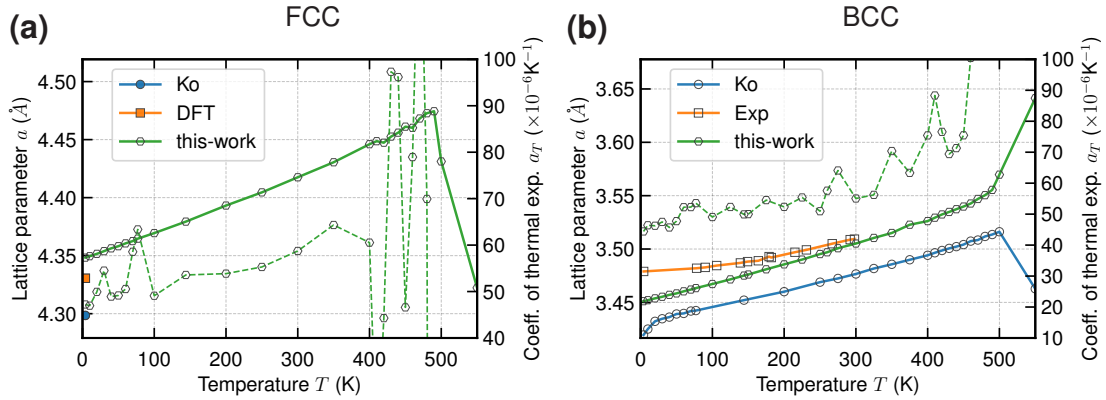

Figure 8: Lattice parameters as a function of temperature of the (a) FCC and (b) BCC structure. The dashed lines are the coefficients of thermal expansion calculated with the new MEAM interatomic potential. The experimental data in (b) are based on Ref. [66] and 0-K value is extrapolated (see Ref. [66]). For the Ko potential, the FCC structure is not stable.

3.8. Elastic constants as a function of temperature

Figure 9 shows the elastic constants of the potential as a function of temperature in comparison with experimental/DFT values and the Ko potential [18]. The new potential exhibits thermal softening in both the FCC and BCC structures. For the BCC structure, all elastic constants are close to extant experimental values between 77 K and 200 K. Above 470 K, its shear modulus C_{44} drops to 0, indicating its melting point is close to 470 K, in agreement with the experimental melting point of 454 K. The Ko potential shows rapid drop in elastic constants from 0 K to 10 K, followed by a gradual increasing of elastic constants from 10 K to 75 K, nearly temperature-independent elastic constants between 75 K to 300 K and thermal softening above 300 K. Its elastic constants C_{44} are also much lower than the experimental values. The elastic constants of the Ko potential in the FCC structure are not calculated since the FCC structure is not stable.

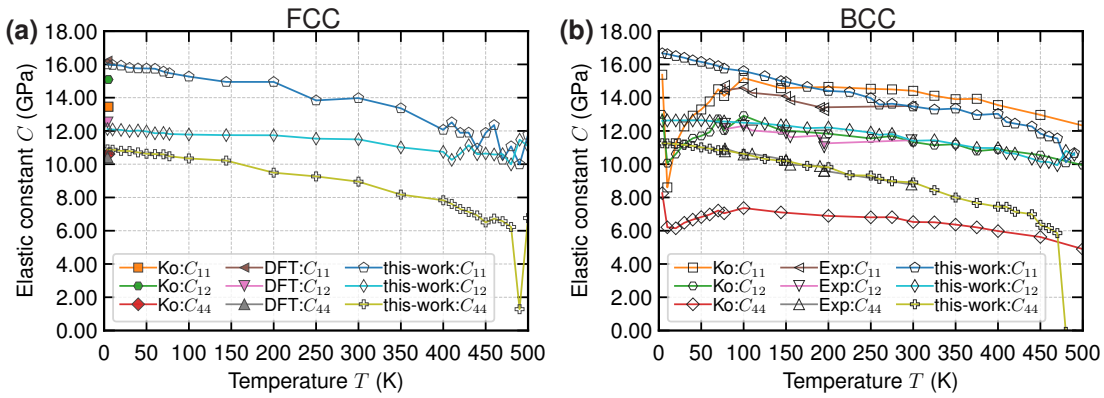

Figure 9: Elastic constants of the (a) FCC and (b) BCC structures at finite temperatures. Experimental and DFT data are from Refs. [67–69] and Ref. [54], respectively.

3.9. Phonon dispersion relations

Figure 10 shows the phonon-dispersion relation of the new potential in comparison with DFT results [1] and the Ko potential. For the BCC phase, both potentials have good matching with DFT at low to medium frequencies in all directions. In particular, quantitative agreement is seen around the Γ point, indicating accurate elastic constants of the BCC phase. At higher frequencies in the N, H, and P directions, the Ko potential is more accurate when compared to DFT values than the new interatomic potential. For the FCC phase, the Ko potential has good agreement with DFT at all frequencies. However, it exhibits modes with imaginary frequencies around the Γ point, suggesting the mechanical instability of the FCC structure in the Ko potential (i.e., $C_{12} > C_{11}$). Both DFT and the new potential do not exhibit such modes.

3.10. Dislocation cores in BCC structures

Figure 11 shows the ⟨111⟩/2 edge and screw dislocation cores in BCC structures of Li. The edge dislocation adopts a non-dissociated core with some spread on the {110} plane, which is consistent with no meta-stable stacking fault seen on this slip plane (Fig. 5). The edge core width is ~10 Å based on the Nye tensor analysis [70, 71]. This core is also qualitatively similar to those of transition metals [71]. The screw dislocation adopts a degenerate core structure as shown in Fig. 11b. The degenerate core has a ⟨111⟩-axis threefold symmetry and has been observed in BCC transition metal alloys [72, 73]. Two variants with identical energy, D_1 and D_2, can be generated by a two-fold rotation along the $[10\bar{1}]$-axis. The degenerate core is distinctly different from the non-degenerate core which possesses both a ⟨111⟩-axis threefold symmetry and a ⟨110⟩ diad axis symmetry seen in all BCC transition metals. The degenerate-core exhibited by the new potential is similar to the core structure calculated by DFT and is fully consistent with a new physics-based χ model (see Ref. [9] for details).

We further investigate the gliding behavior of the screw dislocation under a shear stress of 20 MPa and at a low temperature of 4 K. The glide behavior is similar at higher temperatures, but is less distinguishable at each critical configurations. Figure 12 shows the trajectory of the screw dislocation and intermediate core structures. Starting from the D_1 core (Fig. 12b), the screw dislocation glides along the $(\bar{1}10)$ plane to the next easy-core (D_2, Fig. 12d) via an intermediate split core configuration (Fig. 12c). Subsequently, the D_2 core glides along the $(\bar{1}01)$ plane via another split core (Fig. 12e) and reaches the D_1 core configuration (Fig. 12f). The D_1 and D_2 cores thus glide on alternative {110} planes, yielding a composite glide behavior with average glide plane along $\{11\bar{2}\}$ planes. The choice of the respective {110} glide planes is dictated by the variants of the degenerate core and the direction of the applied driving stress. Equivalently, the D_1 core can glide on the $(0\bar{1}1)$ plane (Fig. 12a) to reach a D_2 configuration, which glides further on a $(\bar{1}01)$ plane, creating another set of composite {112} glides. The above glide behavior is fully consistent with that of degenerate core seen in BCC transition metal alloys [9, 74].

3.11. Free energies of FCC, BCC and HCP structures

Figure 13 shows the relative free energies of FCC, BCC and HCP Li as a function of temperature under zero pressure in comparison with DFT-based calculations [75]. For the current potential, the free energies are calculated using the non-equilibrium Hamiltonian integration method with two different paths (FL and RS, see Section 2.7). The two different paths yield nearly identical results; the differences are on the order of 10^{-2} meV/atom and the accuracies are sufficient for us to determine the relative stability of all three

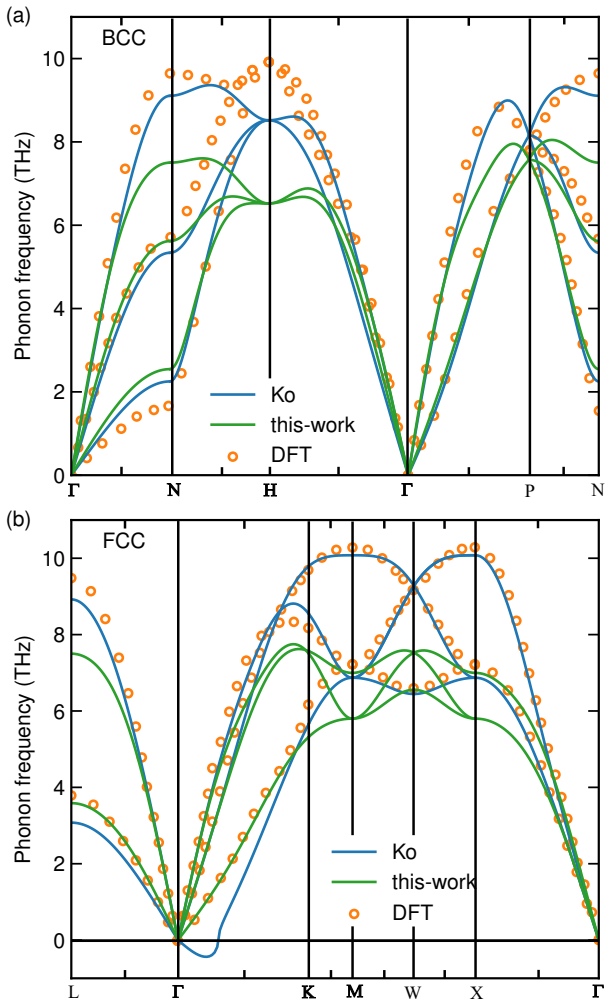

Figure 10: Phonon spectra of (a) the BCC and (b) FCC structures calculated by the new MEAM interatomic potential and the Ko potential [18]. The DFT data are from the work of Ackland et al. [1]

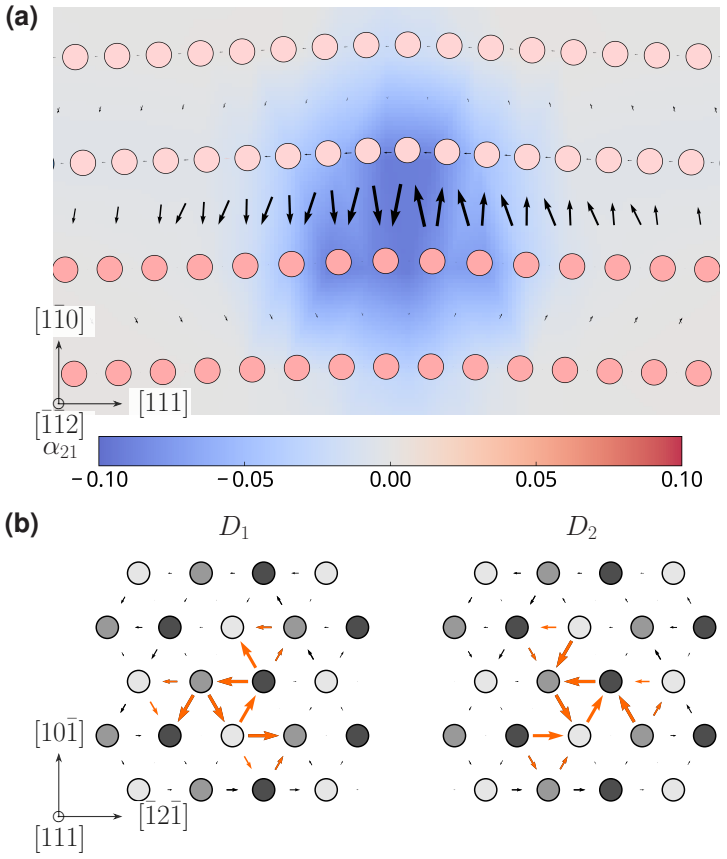

Figure 11: The ⟨111⟩/2 dislocation core structures on the {110} plane in BCC Li predicted by the new MEAM interatomic potential. (a) Edge dislocation. (b) Screw dislocation. In (a), the color contour represents the Nye tensor component α_{21}. The arrows are the differential displacements (DD) and The screw dislocation adopts a degenerate core structure with two variants D_1 and D_2 possessing a ⟨111⟩-axis 3-fold symmetry.

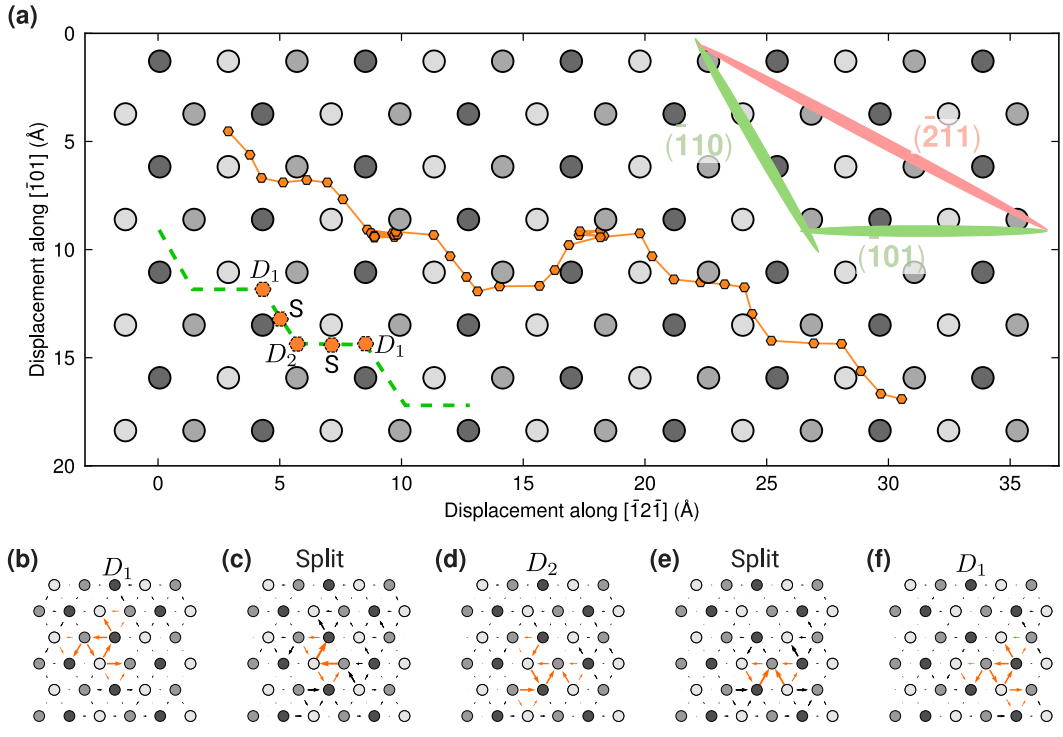

Figure 12: Gliding of the screw dislocation core under a shear stress of 20 MPa at 4 K. (a) Trajectory of the screw dislocation. The orange solid line represents the path of the core and each point is the core center determined by the Nye tensor screw component α_{31} [71]. The green dashed line is a schematic illustration of the alternating {110} slip with an average {112} slip. The respective cores (D_1, S, D_2) are shown in (b-f).

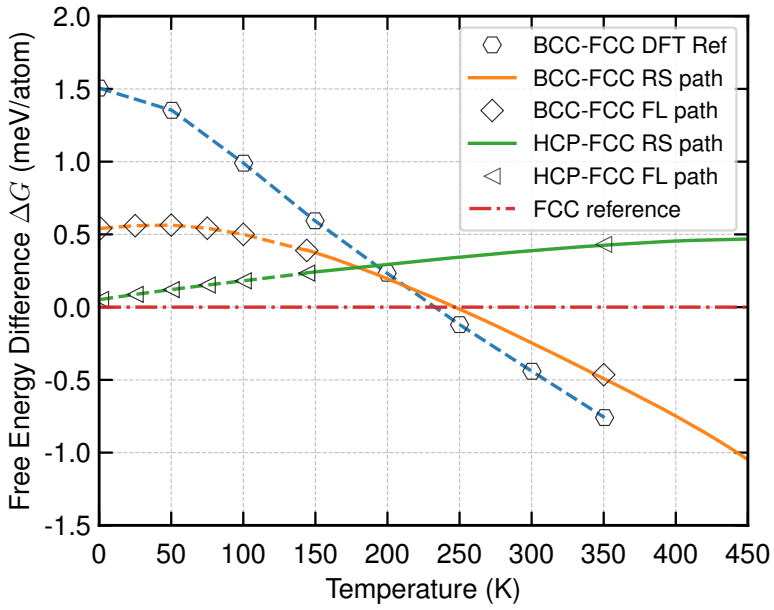

Figure 13: Relative free energies of the FCC, BCC and HCP structure as a function of temperature under zero pressure conditions calculated by the new MEAM interatomic potential. For clarity, the free energies are reported using that of the FCC structure as references. The discrete points denote calculations based on the Frenkel-Ladd (FL) path and solid lines denote calculations based on the Reversible Scaling (RS) path. DFT data is extracted from Ref. [75]

solid phases. This is perhaps largely due to the fact that all three phases are at least metastable in the entire temperature range.

The free energy calculation shows that FCC is the thermodynamic stable phase at low temperatures. The energy difference between the BCC and FCC phases $\Delta G^{\text{BCC-FCC}}$ generally decreases with increasing temperature and the BCC phase becomes the thermodynamic stable phase at 247 K, which is close to the phase transition temperature of 233 K from DFT-based calculations. The BCC phase is stable afterwards and upto the melting point of ~470 K as determined based on the criterion of $C_{44} = 0$. The HCP phase is always metastable relative to the FCC phase throughout the entire temperature range. The free energy difference between the HCP and FCC phases increases with increasing temperature. Its free energy is in between the BCC and FCC phases upto 180 K where the BCC phase becomes more favorable relative to the HCP phase. We note that $\Delta G^{\text{BCC-FCC}}$ of the new potential is close to that of DFT-based calculations between 150 K and 350 K. The discrepancy becomes larger at lower temperatures, particularly below 150 K where quantum mechanics effects become important (the Debye temperature of Li is 335 K). Since the classical interatomic potential does not contain quantum mechanics information, it naturally does not capture this low-temperature behavior.

3.12. Phase transformation in temperature cycling

Li exhibits allotropic phase transformation among the BCC, FCC and rhombohedral 9R structures at different temperatures. Such phase transformations have been previously demonstrated using the Ko potential and in the work by Ackland et al [1]. We have repeated MD simulations under temperature cycling with the same thermodynamic conditions and supercell dimensions as that used by Ko et al [18]. The Ko potential does show phase transformations as described in Ref. [18] However, phase transformation is not seen in MD simulations using a larger supercell dimension of 4.4 nm × 4.4 nm × 19.9 nm. Furthermore, the FCC phase is not stable even at low temperatures (e.g., 10 K) during measurements of lattice parameter and elastic constants (see Section. 3.8). Therefore, the phase transformation exhibited by the Ko potential may be very sensitive to simulation conditions, such as supercell sizes, and may not reveal the true physical behavior of Li.

To demonstrate phase transformation of the current potential, we use a larger, fully periodic simulation supercell of dimension 10 nm × 10 nm × 5 nm. The supercell is populated with 15 randomly oriented grains of FCC Li. We used a relatively small supercell with a polycrystalline microstructure since all three crystal structures (FCC, BCC and HCP) are mechanically stable (Table 4) and solid-to-solid phase transformation via homogeneous nucleation may not be practical within a few nanoseconds in MD simulations. The

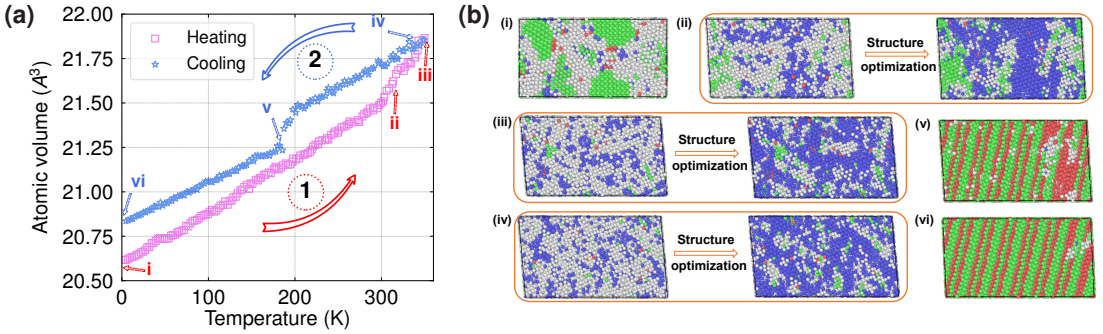

Figure 14: (a) Evolution of atomic volumes during thermal cycling started with an FCC polycrystal (i) at 4 K and ramped to 350 K (ii, iii), followed by cooling to 4 K (iv, v, vi). (b) Atomic structure in thermal cycling in (a). In subpanels ii, iii and vi, the optimized structures following 50 steps of conjugate gradient energy minimization are shown to better illustrate the corresponding crystal structures at relatively high temperatures. Atoms are colored based on their local atomic structure identified by the common neighbor analysis (CNA [62]): FCC-green, BCC-blue, HCP-red, others-white. The FCC structure transforms to BCC at 300 K during temperature ramping. The BCC structure transforms to a FCC/HCP composite structure at 180 K during cooling.

grain boundaries thus provide heterogeneous nucleate sites with lower nucleation barriers, enabling explicit demonstration of the phase transition.

MD simulations are started at 4 K and the temperature is first ramped to 350 K at 125 K/ns, followed by decreasing to 4 K at the same rate and under zero stress conditions. Figure 14 shows the atomic volume and structure as a function of temperature during the above thermal cycling. FCC Li is stable at low temperatures and starts to transform to the BCC phase at 300 K. The transformation nearly completes with most atoms having BCC local atomic structures at 350 K. During the transformation, the initial nanoscale polycrystalline microstructure has also undergone substantial grain boudary migration and grain coarsening. Note that some local regions of FCC structure remained and may have served as the nucleation seeds for the BCC to FCC transformation during the cooling cycle. Along the cooling path, the transformed BCC phase is stable upto 200 K and then starts a relatively quick transformation to a structure characterised by a combination of FCC and HCP structures (ABC and AB stacking sequences). This composite structure is a single crystal structure similar to those obtained by Ko et al. [18]. The exact stacking sequence depends on the simulation cell dimension, shape and thermal paths. In addition, the phase transformation exhibits some hysteresis with mean transition temperature at 250 K, in perfect agreement with the phase transition point determined by free energy calculations (Fig. 13). The current new interatomic potential thus can reproduce several phase transitions similar to those in experiments [1], although the transition temperatures are higher.

4. Discussion and Conclusion

We have used the PSO algorithm to develop a new interatomic potential for Li, using the classical MEAM. Given the complex thermodynamic behavior of Li, properties of all three fundamental solid phases (FCC, BCC and HCP) are used as target properties during the fitting process. This approach has led to an accurate interatomic potential able to reproducing nearly all basic properties of Li, both inside and outside the fitting dataset. The classical MEAM has advantages in several aspects, such as high computational efficiency, ease of use and tunability. Through the extensive testing and validation, the new potential is shown to be suitable for modeling many thermodynamic and mechanical properties of Li in multiple phases and across a wide range of temperatures. The potential applications include study of plastic deformation and fracture in the BCC phase, martensitic phase transformation between the BCC and HCP/FCC structures, diffusion and deposition processes. The success in modeling multi-phase properties is perhaps largely due to the relatively simple electronic structure of Li, which is seen in the Ko potential as well.

The current accurate potential for pure Li has also established a firm foundation for developing potentials for alloys, such as the Al-Li and Mg-Li classes of technological importance. The same approach may be extended to other alkaline metals such as K and Na, which share similar features such as relatively simple electronic structure and small energy differences between the FCC and BCC phases. The current potential exhibits shortcomings on some properties at low temperatures relative to experiments and DFT. For example, the energy difference $\Delta E^{\text{BCC-FCC}}$ between the FCC and BCC phases is smaller than that of the corresponding DFT value. Lower $\Delta E^{\text{BCC-FCC}}$ is chosen to produce the phase transition at a temperature as close to the experimental value as possible. Despite this effort in the fitting process, the current potential has a BCC-to-FCC phase transition point of 247 K similar to that of DFT-based calculations, while experimen-

tal studies generally suggest the BCC phase is not stable and transforms to a meta-stable 9R phase below 150 K [76]. Such deficiencies largely arise from the fact that phase transition temperatures depend on the free energy differences among competing phases and are sensitive to material models, making interatomic potential development particularly challenging for multiphase materials (see, e.g., Ref. [77]). Nevertheless, the BCC-to-Liquid phase transition point is accurately reproduced by the current MEAM potential. The low-temperature deficiencies are exhibited in other properties as well. The MEAM potential, like most others, exhibits positive slope (negative entropy) in the Gibbs free energy vs temperature relation at low temperatures (not shown). It has a non-zero coefficient of thermal expansion α_{T} when the temperature approaches 0 K, while the third law of thermodynamics dictates $\alpha_{\mathrm{T}} \to 0$ as $T \to 0$ K in all materials. Such deficiencies may thus be a true manifestation of the limitations of classical mechanics at low temperatures. Further optimization of the MEAM potential may lead to a better BCC-to-FCC transition temperature and reproduce the low-temperature transition point phenomenologically.

The path towards multi-phase interatomic potentials is obviously more challenging for transition metals, and will require further development in the interatomic potential formulation. The current fitting procedure, such as including multiple phase properties in the fitting dataset and employing an automated parameter optimization algorithm, is general and robust. This approach has been applied to the development of a new interatomic potential for the BCC transition metal vanadium. Our preliminary results show again the robustness and transferability of the MEAM formulation. These new results will be reported separately in a future work.

5. Acknowledgements

This work is supported by the City University of Hong Kong New Research Initiatives (9610436), Research Grants Council, Hong Kong SAR through the Early Career Scheme Fund under project number 21205019 and Collaborative Research Fund under project number 8730054. BY acknowledges the support from Zhejiang University. Computational resources are provided by the Computing Services Centre, City University of Hong Kong.

6. Data and materials availability

The interatomic potential files are available in the Supplementary Materials.

References

[1] G. J. Ackland, M. Dunuwille, M. Martinez-Canales, I. Loa, R. Zhang, S. Sinogeikin, W. Cai, S. Deemyad, Quantum and isotope effects in lithium metal, Science 356 (6344) (2017) 1254. doi:10.1126/science.aal4886.

[2] W. Pichl, M. Krystian, Martensitic transformation and mechanical deformation of high-purity lithium, Materials Science and Engineering: A 273–275 (1999) 208–212. doi:10.1016/S0921-5093(99)00372-X.

[3] M. Hanfland, K. Syassen, N. E. Christensen, D. L. Novikov, New high-pressure phases of lithium, Nature 408 (6809) (2000) 174–178. doi:10.1038/35041515.

[4] C. Xu, Z. Ahmad, A. Aryanfar, V. Viswanathan, J. R. Greer, Enhanced strength and temperature dependence of mechanical properties of Li at small scales and its implications for Li metal anodes, Proceedings of the National Academy of Sciences 114 (1) (2017) 57–61. doi:10.1073/pnas.1615733114.

[5] K. J. Kim, J. Wortman, S.-Y. Kim, Y. Qi, Atomistic simulation derived insight on the irreversible structural changes of si electrode during fast and slow delithiation, Nano Letters 17 (7) (2017) 4330–4338. doi:10.1021/acs.nanolett.7b01389.

[6] J. Mendez, M. Ponga, M. Ortiz, Diffusive molecular dynamics simulations of lithiation of silicon nanopillars, Journal of the Mechanics and Physics of Solids 115 (2018) 123–141. doi:10.1016/j.jmps.2018.03.008.

[7] L. A. Selis, J. M. Seminario, Dendrite formation in Li-metal anodes: an atomistic molecular dynamics study, RSC Advances 9 (48) (2019) 27835–27848. doi:10.1039/c9ra05067a.

[8] B. Ghalami Choobar, H. Modarress, R. Halladj, S. Amjad-Iranagh, Electrodeposition of lithium metal on lithium anode surface, a simulation study by: Kinetic Monte Carlo-embedded atom method, Computational Materials Science 192 (2021) 110343. doi:10.1016/j.commatsci.2021.110343.

[9] R. Wang, L. Zhu, S. Pattamatta, S. D. J., Z. Wu, Revealing and controlling the core of screw dislocations in bcc metals, under review (2021). doi:10.21203/rs.3.rs-879826/v1.

[10] M. S. Daw, M. I. Baskes, Embedded-atom method: Derivation and application to impurities, surfaces, and other defects in metals, Physical Review B 29 (12) (1984) 6443–6453. doi:10.1103/physrevb.29.6443.

[11] M. I. Baskes, Application of the embedded-atom method to covalent materials: A semiempirical potential for silicon, Physical Review Letters 59 (23) (1987) 2666–2669. doi:10.1103/PhysRevLett.59.2666.

[12] M. I. Baskes, J. S. Nelson, A. F. Wright, Semiempirical modified embedded-atom potentials for silicon and germanium, Physical Review B 40 (9) (1989) 6085–6100. doi:10.1103/PhysRevB.40.6085.

[13] B.-J. Lee, M. I. Baskes, H. Kim, Y. Koo Cho, Second nearest-neighbor modified embedded atom method potentials for bcc transition metals, Physical Review B 64 (18) (2001) 184102–11. doi:10.1103/PhysRevB.64.184102.

[14] Y.-M. Kim, I.-H. Jung, B.-J. Lee, Atomistic modeling of pure Li and Mg–Li system, Modelling and Simulation in Materials Science and Engineering 20 (3) (2012) 035005–13. doi:10.1088/0965-0393/20/3/035005.

[15] Z. Cui, F. Gao, Z. Cui, J. Qu, A second nearest-neighbor embedded atom method interatomic potential for Li–Si alloys, Journal of Power Sources 207 (2012) 150–159. doi:10.1016/j.jpowsour.2012.01.145.
[16] M. Alam, S. Groh, Dislocation modeling in bcc lithium: A comparison between continuum and atomistic predictions in the modified embedded atoms method, Journal of Physics and Chemistry of Solids 82 (2015) 1–9. doi:10.1016/j.jpcs.2015.02.007.
[17] S. Groh, M. Alam, Fracture behavior of lithium single crystal in the framework of (semi-)empirical force field derived from first-principles, Modelling and Simulation in Materials Science and Engineering 23 (4) (2015) 045008–23. doi:10.1088/0965-0393/23/4/045008.
[18] W.-S. Ko, J. B. Jeon, Interatomic potential that describes martensitic phase transformations in pure lithium, Computational Materials Science 129 (2017) 202–210. doi:10.1016/j.commatsci.2016.12.018.
[19] A. Nichol, G. J. Ackland, Property trends in simple metals: An empirical potential approach, Physical Review B 93 (18) (2016) 184101. doi:10.1103/physrevb.93.184101.
[20] Y. Zuo, C. Chen, X. Li, Z. Deng, Y. Chen, J. Behler, G. Csányi, A. V. Shapeev, A. P. Thompson, M. A. Wood, et al., Performance and cost assessment of machine learning interatomic potentials, The Journal of Physical Chemistry A 124 (4) (2020) 731–745. doi:10.1021/acs.jpca.9b08723.
[21] F. Mouhat, F.-X. Coudert, Necessary and sufficient elastic stability conditions in various crystal systems, Physical Review B 90 (22) (2014) 224104–4. doi:10.1103/physrevb.90.224104.
[22] A. P. Thompson, H. M. Aktulga, R. Berger, D. S. Bolintineanu, W. M. Brown, P. S. Crozier, P. J. in 't Veld, A. Kohlmeyer, S. G. Moore, T. D. Nguyen, R. Shan, M. J. Stevens, J. Tranchida, C. Trott, S. J. Plimpton, LAMMPS - a flexible simulation tool for particle-based materials modeling at the atomic, meso, and continuum scales, Computer Physics Communications 271 (2022) 108171. doi:10.1016/j.cpc.2021.108171.
[23] J. Kennedy, R. Eberhart, Particle swarm optimization, Proceedings of ICNN'95 - International Conference on Neural Networks (1995) 1942–1948doi:10.1109/icnn.1995.488968.
[24] G. Kresse, J. Furthmüller, Efficiency of ab-initio total energy calculations for metals and semiconductors using a plane-wave basis set, Computational Materials Science 6 (1) (1996) 15–50. doi:10.1016/0927-0256(96)00008-0.
[25] G. Kresse, J. Furthmüller, Efficient iterative schemes forab initiototal-energy calculations using a plane-wave basis set, Physical Review B 54 (16) (1996) 11169–11186. doi:10.1103/physrevb.54.11169.
[26] G. Kresse, D. Joubert, From ultrasoft pseudopotentials to the projector augmented-wave method, Physical Review B 59 (3) (1999) 1758–1775. doi:10.1103/PhysRevB.59.1758.
[27] J. P. Perdew, K. Burke, M. Ernzerhof, Generalized gradient approximation made simple, Physical Review Letters 77 (18) (1996) 3865–3868. doi:10.1103/physrevlett.77.3865.
[28] P. E. Blöchl, Projector augmented-wave method, Physical Review B 50 (24) (1994) 17953–17979. doi:10.1103/PhysRevB.50.17953.
[29] M. Methfessel, A. T. Paxton, High-precision sampling for Brillouin-zone integration in metals, Physical Review B 40 (6) (1989) 3616–3621. doi:10.1103/physrevb.40.3616.
[30] H. J. Monkhorst, J. D. Pack, Special points for Brillouin-zone integrations, Physical Review B 13 (12) (1976) 5188–5192. doi:10.1103/PhysRevB.13.5188.
[31] J. A. Nieminen, A. P. Sutton, J. B. Pethica, Static junction growth during frictional sliding of metals, Acta Metallurgica et Materialia 40 (10) (1992) 2503–2509. doi:10.1016/0956-7151(92)90320-E.
[32] A. P. Sutton, R. W. Balluffi, Interfaces in Crystalline Materials, Clarendon Press, 1995.
[33] S. Kibey, J. B. Liu, D. D. Johnson, H. Sehitoglu, Generalized planar fault energies and twinning in Cu–Al alloys, Applied Physics Letters 89 (19) (2006) 191911–3. doi:10.1063/1.2387133.
[34] B. Yin, Z. Wu, W. A. Curtin, Comprehensive first-principles study of stable stacking faults in hcp metals, Acta Materialia 123 (2017) 223–234. doi:10.1016/j.actamat.2016.10.042.
[35] M. I. Baskes, Modified embedded-atom potentials for cubic materials and impurities, Physical Review B 46 (5) (1992) 2727–2742. doi:10.1103/PhysRevB.46.2727.
[36] B.-J. Lee, M. I. Baskes, Second nearest-neighbor modified embedded-atom-method potential, Physical Review B 62 (13) (2000) 8564–8567. doi:10.1103/PhysRevB.62.8564.
[37] V. Bulatov, W. Cai, Computer Simulations of Dislocations, Oxford University Press, USA, 2006. doi:10.1093/oso/9780198526148.001.0001.
[38] A. Togo, I. Tanaka, First principles phonon calculations in materials science, Scripta Materialia 108 (2015) 1–5. doi:10.1016/j.scriptamat.2015.07.021.
[39] A. Carreras, Phonolammps (2022).
URL https://github.com/abelcarreras/phonolammps
[40] J. G. Kirkwood, Statistical mechanics of fluid mixtures, The Journal of Chemical Physics 3 (5) (1935) 300–313. doi:10.1063/1.1749657.
[41] C. Vega, E. Sanz, J. L. F. Abascal, E. G. Noya, Determination of phase diagrams via computer simulation: methodology and applications to water, electrolytes and proteins, Journal of Physics: Condensed Matter 20 (15) (2008) 153101. doi:10.1088/0953-8984/20/15/153101.
[42] M. Watanabe, W. P. Reinhardt, Direct dynamical calculation of entropy and free energy by adiabatic switching, Physical Review Letters 65 (26) (1990) 3301–3304. doi:10.1103/physrevlett.65.3301.
[43] M. de Koning, A. Antonelli, Einstein crystal as a reference system in free energy estimation using adiabatic switching, Physical Review E 53 (1) (1996) 465–474. doi:10.1103/PhysRevE.53.465.
[44] C. Jarzynski, Nonequilibrium equality for free energy differences, Physical Review Letters 78 (1997) 2690–2693. doi:10.1103/PhysRevLett.78.2690.
[45] R. Freitas, M. Asta, M. de Koning, Nonequilibrium free-energy calculation of solids using LAMMPS, Computational Materials Science 112 (2016) 333–341. doi:10.1016/j.commatsci.2015.10.050.
[46] M. de Koning, Optimizing the driving function for nonequilibrium free-energy calculations in the linear regime: A variational approach, The Journal of Chemical Physics 122 (10) (2005) 104106. doi:10.1063/1.1860556.
[47] D. Frenkel, A. J. C. Ladd, New Monte Carlo method to compute the free energy of arbitrary solids. Application to the fcc and hcp phases of hard spheres, The Journal of Chemical Physics 81 (7) (1984) 3188–3193. doi:10.1063/1.448024.
[48] M. de Koning, A. Antonelli, S. Yip, Optimized free-energy evaluation using a single reversible-scaling simulation, Physical Review Letters 83 (20) (1999) 3973–3977. doi:10.1103/PhysRevLett.83.3973.

[49] F. Faglioni, B. V. Merinov, W. A. Goddard, Room-temperature lithium phases from density functional theory, The Journal of Physical Chemistry C 120 (48) (2016) 27104–27108. doi:10.1021/acs.jpcc.6b08168.
[50] W. M. Haynes (Ed.), CRC Handbook of Chemistry and Physics, CRC Press, 2014. doi:10.1201/b17118.
[51] R. Tran, Z. Xu, B. Radhakrishnan, D. Winston, W. Sun, K. A. Persson, S. P. Ong, Surface energies of elemental crystals, Scientific Data 3 (2016) 160080. doi:10.1038/sdata.2016.80.
[52] T. Angsten, T. Mayeshiba, H. Wu, D. Morgan, Elemental vacancy diffusion database from high-throughput first-principles calculations for fcc and hcp structures, New Journal of Physics 16 (1) (2014) 015018. doi:10.1088/1367-2630/16/1/015018.
[53] A. Jain, S. P. Ong, G. Hautier, W. Chen, W. D. Richards, S. Dacek, S. Cholia, D. Gunter, D. Skinner, G. Ceder, K. A. Persson, Commentary: The materials project: A materials genome approach to accelerating materials innovation, APL Materials 1 (1) (2013) 011002. doi:10.1063/1.4812323.
[54] M. de Jong, W. Chen, H. Geerlings, M. Asta, K. A. Persson, A database to enable discovery and design of piezoelectric materials, Scientific Data 2 (1) (2015) 150053. doi:10.1038/sdata.2015.53.
[55] M. Jäckle, A. Groß, Microscopic properties of lithium, sodium, and magnesium battery anode materials related to possible dendrite growth, The Journal of Chemical Physics 141 (17) (2014) 174710. doi:10.1063/1.4901055.
[56] E. J. Covington, D. J. Montgomery, Lattice constants of separated lithium isotopes, The Journal of Chemical Physics 27 (5) (1957) 1030–1032. doi:10.1063/1.1743926.
[57] C. Kittel, Wiley, 2005.
[58] R. A. Felice, J. Trivisonno, D. E. Schuele, Temperature and pressure dependence of the single-crystal elastic constants of ^{6}Li and natural lithium, Physical Review B 16 (12) (1977) 5173–5184. doi:10.1103/PhysRevB.16.5173.
[59] W. R. Tyson, W. A. Miller, Surface free energies of solid metals: Estimation from liquid surface tension measurements, Surface Science 62 (1) (1977) 267–276. doi:10.1016/0039-6028(77)90442-3.
[60] R. Feder, Equilibrium defect concentration in crystalline lithium, Physical Review B 2 (4) (1970) 828–834. doi:10.1103/physrevb.2.828.
[61] Z. Wu, M. F. Francis, W. A. Curtin, Magnesium interatomic potential for simulating plasticity and fracture phenomena, Modelling and Simulation in Materials Science and Engineering 23 (1) (2015) 015004. doi:10.1088/0965-0393/23/1/015004.
[62] D. Faken, H. Jónsson, Systematic analysis of local atomic structure combined with 3d computer graphics, Computational Materials Science 2 (2) (1994) 279–286. doi:10.1016/0927-0256(94)90109-0.
[63] V. Vitek, Multilayer stacking faults and twins on {211} planes in B.C.C. metals, Scripta Metallurgica 4 (9) (1970) 725–732. doi:10.1016/0036-9748(70)90214-0.
[64] A. H. Faisal, C. R. Weinberger, Modeling twin boundary structures in body centered cubic transition metals, Computational Materials Science 197 (2021) 110649. doi:10.1016/j.commatsci.2021.110649.
[65] ASM International, 2002.
[66] T. N. Mel'nikova, A. G. Mozgovoi, Lithium isotope density and thermal expansion, High Temperature 26 (6) (1989) 848–854.
[67] H. C. Nash, C. S. Smith, Single-crystal elastic constants of lithium, Journal of Physics and Chemistry of Solids 9 (2) (1959) 113–118. doi:10.1016/0022-3697(59)90201-x.
[68] J. Trivisonno, C. S. Smith, Elastic constants of lithium-magnesium alloys, Acta Metallurgica 9 (12) (1961) 1064–1071. doi:10.1016/0001-6160(61)90175-4.
[69] T. Slotwinski, J. Trivisonno, Temperature dependence of the elastic constants of single crystal lithium, Journal of Physics and Chemistry of Solids 30 (5) (1969) 1276–1278. doi:10.1016/0022-3697(69)90386-2.
[70] C. S. Hartley, Y. Mishin, Characterization and visualization of the lattice misfit associated with dislocation cores, Acta Materialia 53 (5) (2005) 1313–1321. doi:10.1016/j.actamat.2004.11.027.
[71] M. R. Fellinger, A. M. Z. Tan, L. G. Hector, D. R. Trinkle, Geometries of edge and mixed dislocations in bcc Fe from first-principles calculations, Physical Review Materials 2 (11) (2018) 113605. doi:10.1103/physrevmaterials.2.113605.
[72] L. Romaner, C. Ambrosch-Draxl, R. Pippan, Effect of rhenium on the dislocation core structure in tungsten, Physical Review Letters 104 (19) (2010) 195503–4. doi:10.1103/physrevlett.104.195503.
[73] G. D. Samolyuk, Y. N. Osetsky, R. E. Stoller, The influence of transition metal solutes on the dislocation core structure and values of the Peierls stress and barrier in tungsten, Journal of Physics: Condensed Matter 25 (2) (2012) 025403–9. doi:10.1088/0953-8984/25/2/025403.
[74] H. Li, S. Wurster, C. Motz, L. Romaner, C. Ambrosch-Draxl, R. Pippan, Dislocation-core symmetry and slip planes in tungsten alloys: Ab initio calculations and microcantilever bending experiments, Acta Materialia 60 (2) (2012) 748–758. doi:10.1016/j.actamat.2011.10.031.
[75] M. Hutcheon, R. Needs, Structural and vibrational properties of lithium under ambient conditions within density functional theory, Physical Review B 99 (1) (2019) 014111. doi:10.1103/physrevb.99.014111.
[76] M. Frost, J. B. Kim, E. E. McBride, J. R. Peterson, J. S. Smith, P. Sun, S. H. Glenzer, High-pressure melt curve and phase diagram of lithium, Physical Review Letters 123 (6) (2019) 065701–5. doi:10.1103/physrevlett.123.065701.
[77] T. Wen, R. Wang, L. Zhu, L. Zhang, H. Wang, D. J. Srolovitz, Z. Wu, Specialising neural network potentials for accurate properties and application to the mechanical response of titanium, npj Computational Materials 7 (1) (2021) 206–11. doi:10.1038/s41524-021-00661-y.